Journal of Applied Physics

Multiscale simulations of the electronic structure of III-nitride quantum wells with varied indium content: Connecting atomistic and continuum-based models

Cite as: J. Appl. Phys. **129**, 073104 (2021); https://doi.org/10.1063/5.0031514
Submitted: 01 October 2020 • Accepted: 27 January 2021 • Published Online: 18 February 2021

D. Chaudhuri, M. O'Donovan, T. Streckenbach, et al.

View Online Export Citation CrossMark

ARTICLES YOU MAY BE INTERESTED IN

From atomistic tight-binding theory to macroscale drift–diffusion: Multiscale modeling and numerical simulation of uni-polar charge transport in (In,Ga)N devices with random fluctuations
Journal of Applied Physics **130**, 065702 (2021); https://doi.org/10.1063/5.0059014

A first-principles understanding of point defects and impurities in GaN
Journal of Applied Physics **129**, 111101 (2021); https://doi.org/10.1063/5.0041506

Atomistic analysis of radiative recombination rate, Stokes shift, and density of states in c-plane InGaN/GaN quantum wells
Applied Physics Letters **116**, 181104 (2020); https://doi.org/10.1063/5.0006128

© 2021 Author(s).

Journal of Applied Physics ARTICLE scitation.org/journal/jap

Multiscale simulations of the electronic structure of III-nitride quantum wells with varied indium content: Connecting atomistic and continuum-based models

Cite as: J. Appl. Phys. **129**, 073104 (2021); doi: 10.1063/5.0031514
Submitted: 1 October 2020 · Accepted: 27 January 2021 ·
Published Online: 18 February 2021

View Online Export Citation CrossMark

D. Chaudhuri,[1,a)] M. O'Donovan,[1,2] T. Streckenbach,[3] O. Marquardt,[3] P. Farrell,[3] S. K. Patra,[1] T. Koprucki,[3] and S. Schulz[1]

AFFILIATIONS

[1]Tyndall National Institute, University College Cork, Cork T12 R5CP, Ireland
[2]Department of Physics, University College Cork, Cork T12 YN60, Ireland
[3]Weierstrass Institute (WIAS), Mohrenstr. 39, 10117 Berlin, Germany

[a)]**Author to whom correspondence should be addressed:** debapriyachaudhuri.jobs@gmail.com

ABSTRACT

Carrier localization effects in III-N heterostructures are often studied in the frame of modified continuum-based models utilizing a single-band effective mass approximation. However, there exists no comparison between the results of a modified continuum model and atomistic calculations on the same underlying disordered energy landscape. We present a theoretical framework that establishes a connection between atomistic tight-binding theory and continuum-based electronic structure models, here a single-band effective mass approximation, and provide such a comparison for the electronic structure of (In,Ga)N quantum wells. In our approach, in principle, the effective masses are the only adjustable parameters since the confinement energy landscape is directly obtained from tight-binding theory. We find that the electronic structure calculated within effective mass approximation and the tight-binding model differ noticeably. However, at least in terms of energy eigenvalues, an improved agreement between the two methods can be achieved by adjusting the band offsets in the continuum model, enabling, therefore, a recipe for constructing a modified continuum model that gives a reasonable approximation of the tight-binding energies. Carrier localization characteristics for energetically low lying, strongly localized states differ, however, significantly from those obtained using the tight-binding model. For energetically higher lying, more delocalized states, good agreement may be achieved. Therefore, the atomistically motivated continuum-based single-band effective mass model established provides a good, computationally efficient alternative to fully atomistic investigations, at least at when targeting questions related to higher temperatures and carrier densities in (In,Ga)N systems.

© 2021 Author(s). All article content, except where otherwise noted, is licensed under a Creative Commons Attribution (CC BY) license (http://creativecommons.org/licenses/by/4.0/). https://doi.org/10.1063/5.0031514

I. INTRODUCTION

In the past two decades, III-N-based semiconductors have attracted significant research interest given their potential for a variety of different applications. These applications include photovoltaic cells and light-emitting diodes (LEDs).[1–3] For instance, the active region of modern LEDs operating in the blue spectral region is based on *c*-plane (In,Ga)N/GaN quantum wells (QWs).[2,4,5] Despite widespread application of these LED structures nowadays, to further improve their overall performance and efficiency, a detailed understanding of their fundamental properties is required, especially when moving into the ultraviolet or the green spectral region.

While theoretical studies can provide guidance to achieve these goals, it is overall a very challenging task. Experimental investigations give clear indications that the electronic and optical properties of III-N materials and heterostructures are strongly affected by carrier localization effects, originating from alloy fluctuations in III-N alloys.[6–9] Thus, to achieve an accurate theoretical description

© Author(s) 2021

of these properties, it is important that the theoretical model accounts for localization effects.[10–15] As a consequence, a fully three-dimensional (3D) model is required, even when studying III-N quantum well (QW) structures. To target carrier localization effects in a such a 3D description, a variety of different theoretical approaches has been applied in the literature. These range from fully atomistic calculations[12,16] to modified continuum-based models.[10,11,17–20] While atomistic modeling has been successfully applied to describe whole devices[21,22] as well as the influence of alloy fluctuations on the electronic properties of semiconductor heterostructures,[13,23] their application generates a huge computational effort, depending on the numbers of atoms involved. This applies, in particular, to the systematic evaluation of trends when modifying dimensions or chemical composition of a semiconductor heterostructure in large simulation cells. Especially in industry focused device design activities, the huge computational effort of full atomistic device calculations is often not a viable route.

Therefore, modified continuum-based approaches have found widespread application to account for alloy fluctuations and, thus, carrier localization effects in, for instance, (In,Ga)N/GaN heterostructures. While the numerical burden in most cases is significantly reduced compared to atomistic approaches, this comes at a cost: the underlying atomistic structure is lost and the calculations are carried out on a mesh where the information about the atomic species is replaced by an average alloy content.

The determination of the local alloy content depends then on the chosen interpolation procedure and the same is true for the (local) material parameters.[18,23] Overall, such an approach raises several questions, including how valid the use of bulk material parameters in small spatial regions are or the fact that small scale alloy fluctuations are in general beyond the validity limits of continuum-based models. Nevertheless, especially single-band effective mass approximations have been often used in the literature to study the electronic and optical properties of (In,Ga)N/GaN QWs with a strongly fluctuating energy landscape, constructed from bulk band parameters. In general, there exist different approaches in the literature for establishing such modified continuum-based models but there exists basically no analysis of how such an approach compares to the outcome of an atomistic model using the same underlying structure. Recent theoretical studies give indications that continuum-based models may underestimate carrier localization effects in (In,Ga)N/GaN QW systems,[24] while, however, excellent agreement between atomistic and continuum-based modeling has been observed for nitride quantum dots of comparatively small dimensions.[25]

In this work, we fill this gap and establish a general theoretical framework that allows us (i) to connect an atomistic tight-binding (TB) model with modified continuum-based approaches (single-band effective mass, multi-band $\mathbf{k}\cdot\mathbf{p}$) and (ii) to directly compare the results of these two approaches on the same input data set. The benefit of this approach is that we establish a modified continuum-based model that can be tailored and adjusted to provide a reasonable agreement with the atomistic model. This lends further trust for the application of this framework in future studies, including, for instance, transport calculations of nitride-based heterostructures.

More specifically, we have developed a method that allows us to extract an energy landscape from the atomistic TB model that accounts for local strain and built-in potential fluctuations, which then serves directly as an input for continuum-based calculations. In doing so, the approach bypasses the complication of using locally averaged material parameters such as bulk band offsets or piezoelectric coefficients since the continuum-based model is directly connected to the TB energy landscape which includes modifications in the band edges due to alloy fluctuations in the active region on a microscopic level. The continuum model, thus, operates on an atomistically derived energy landscape. Additionally, when connecting TB and single-band effective mass approximation (EMA), in principle, the only adjustable parameters left are the electron and hole effective masses. Furthermore, to transfer the atomistic energy landscape into the continuum-based model, we use a finite element mesh (FEM) with as many nodes as lattice sites. Overall, our approach allows for multiscale modeling[26–28] of the electronic and optical properties of III-N heterostructures in the picture of a modified continuum model with a benchmark loop to atomistic calculations. This, therefore, enables us to adjust the model to design an "atomistically corrected" continuum model. In future studies, this may facilitate transport studies by using drift-diffusion calculations to (i) account for alloy fluctuations and (ii) to allow for drastically reduced computational efforts when comparing to full atomistic device calculations.

We show that even after calibrating the EMA against a virtual crystal approximation (VCA) TB model, the transition energies predicted by the EMA for the random alloy case significantly deviates from the TB results. This discrepancy is larger with increasing In content, i.e., for longer wavelengths. However, we will show that while preserving the average energetic separation between electron and hole states, a very good agreement between TB and EMA is achieved when the band offset in the (In,Ga)N region (QW region) is adjusted by a rigid shift that increases with increasing In content. This shows that the established framework can now be adjusted to give a good approximation of the TB results in terms of the energies, which allows us to use it for future calculations. In addition to comparing energy eigenvalues, we have also analyzed carrier localization effects predicted by the two above mentioned methods. To do so, we have calculated inverse participation ratios (IPRs)[7,29] for the first ten electron and hole states within TB and EMA. Our calculations show that in comparison to the TB model, the EMA significantly underestimates hole localization effects, especially for higher In content systems. For electrons, especially for lower In contents, the situation is slightly different and a better agreement between TB and EMA is observed. However, this is only the case for the model that includes the rigid band offset shift. Nevertheless, we also find that the agreement between TB and continuum-based model in terms of carrier localization effects improves for energetically higher lying states. Thus, the developed and established model should provide an attractive approach to investigate (In,Ga)N/GaN QW systems at elevated temperatures and higher carrier densities where energetically high lying states become populated.

The paper is organized as follows: in Sec. II, we introduce the theoretical framework that connects the atomistic and continuum-based models. The calibration of the EMA against the VCA TB model is presented in Sec. III A. Next, in Sec. III B, we compare the energy eigenvalues of the calibrated EMA with TB data for (In,Ga)N/GaN QW systems with 5%, 10%, 15%, and 25%

© Author(s) 2021

In, which exhibit random alloy fluctuations. The average normalized IPR values ($\widetilde{\mathrm{IPR}}$) for first ten electron and hole states in these systems are discussed and presented in Sec. III C. In Sec. IV, we summarize our findings, while in the Appendix, details of our IPR value calculations are given.

II. THEORETICAL FRAMEWORK FOR CONNECTING ATOMISTIC THEORY AND CONTINUUM-BASED MODELS

The aim of our study is to derive a modified continuum-based model that directly incorporates input from atomistic TB theory. In general, to study electronic and optical properties of a semiconductor heterostructure, one is conventionally left with solving Schrödinger's equation,

$$\hat{H}\psi = (\hat{T} + \hat{V})\psi = E\psi, \tag{1}$$

where $\hat{H}$ is the Hamiltonian of the system under consideration, and $\hat{T}$ and $\hat{V}$ are the kinetic and potential energy operators, respectively. The eigenenergy is denoted by E, and ψ is the corresponding eigenstate.

The aim of our framework is to extract a potential energy landscape $\hat{V}$ from an atomistic TB model that can be used in a robust and computationally inexpensive continuum-based description of Eq. (1). The procedure of extracting $\hat{V}$ from a TB model is explained in Sec. II A. In Sec. II B, we outline how the obtained landscape is transferred to a FEM mesh and, thus, prepared for a continuum-based solver. A schematic illustration of the workflow is displayed in Fig. 1. Here, we solve Schrödinger's equation within the framework of a single-band EMA, which has been implemented in the highly flexible plane wave based software package SPHInX,[30–33] which is briefly explained in Sec. II C. We note that for the sake of a simplified discussion, and since it is a widely used approach in the literature to study the impact of alloy fluctuations on the electronic structure of (In,Ga)N QWs, we have limited ourself to a single-band EMA model. Of course, more sophisticated continuum models such as the eight-band $\mathbf{k}\cdot\mathbf{p}$ approach will facilitate a more accurate description of the electronic properties of heterostructures containing alloy fluctuations. For instance, it may be of particular importance to take into account the nonparabolic behavior of the bands, which may become relevant in small structures with large band offset, e.g., small clusters with large

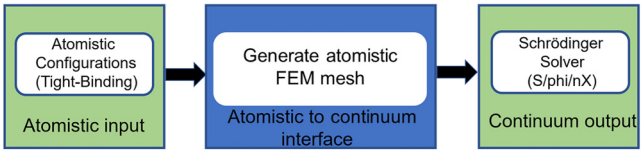

FIG. 1. Schematic workflow from of our theoretical framework to connect an atomistic tight-binding model to a continuum-based Schrödinger solver (here SPHInX). The connection between the atomistic and continuum-based grid is achieved by the finite element method, generating an atomistic finite element mesh that has as many nodes as atomic sites and which is here interpolated on an equidistant tensor-poduct mesh compatible with SPhinX.

In contents. However, the flexibility of SPHInX allows in principle to easily change the underlying Hamiltonian used in solving Schrödinger's equation so that the general approach presented here can be transferred to employ more sophisticated models. Additionally, given that single-band effective mass models are often applied to study carrier localization effects in (In,Ga)N systems, any problem arising from the fact that a strongly fluctuating energy landscape presents in general a challenge for continuum-based models, should be revealed by the analysis presented in this work.

In addition to turning to multi-band $\mathbf{k}\cdot\mathbf{p}$ models and to avoid solving large scale eigenvalue problems, future studies may use the established framework to combine the TB energy landscape, mapped on a FEM mesh, as input for the recently introduced localization landscape theory[18,34] to obtain an effective potential and the localized states on this landscape. All this can then serve, for example, as a starting point for transport calculations in future studies.

A. Tight-binding model and local band edge calculations

Atomistic theoretical studies have already shown that a single In–N–In chain, embedded in GaN, is sufficient to localize hole wave functions in an (In,Ga)N alloy.[7,35] This indicates that in order to capture the localization effects in III-N systems accurately, the theoretical model ideally operates on an atomistic level. While density functional theory (DFT) provides such an atomistic and very accurate description, the computational demand of standard DFT approaches allows only to study systems of a few thousand atoms. Given that for QW or multi-QW systems not only the active QW region but also the barrier material needs to be included, plus sufficiently large in-plane dimensions, the relevant part of the system under consideration easily exceeds 10 000 atoms.

Thus, to capture effects such as random alloy fluctuations on a microscopic level, we apply a nearest neighbor sp^3 TB. The model is described in detail in previous works[36,37] and we only briefly summarize its main ingredients. TB parameters are obtained by fitting the TB band structures to III-N hybrid-functional DFT band structures as discussed in Refs. 38–40. As shown in the above references, the model has also been benchmarked for alloyed systems, by comparing, for example, the bandgap bowing of InGaN or InAlN systems with DFT and/or experimental data. In the case of an alloy, care must be taken when treating the TB matrix elements. Since for the cation sites (Ga, In) the nearest neighbors are always nitrogen atoms, there is no ambiguity in assigning the TB on-site and nearest neighbor matrix elements. This classification is more difficult for nitrogen atoms. In this case, the nearest neighbor environment is a combination of In and Ga atoms. Here, we apply the widely used approach of using weighted averages for the on-site energies according to the number of In and Ga atoms.[41,42] Furthermore, the model accounts for local strain and polarization fields obtained from a valence force field (VFF)[43] model and a local polarization theory, respectively.[38] This model has been extensively tested and compared with experimental and DFT data for both bulk and QW systems.[38,40] As outlined above, the aim of our study is to establish a connection between the atomistic TB model and a continuum-based approach. The idea is to extract an energy

© Author(s) 2021

landscape from TB that can be used as input for the continuum-based calculations. We stress that previous studies that establish and use modified single-band models for (In,Ga)N-based QWs define locally compositionally averaged material parameters such as band offsets or piezoelectric coefficients. There is obviously no gurantee that this represents a good and valid approximation. Our approach is different in the sense that we use a microscopic description of the energy landscape the carriers are "seeing" in a disordered alloy. As we have already shown previously, this results, for example, in a bowing of valence and conduction bad edges due to strain and built-in field fluctuations. Such bowing is usually not accounted for in modified continuum-based approximations. Thus, we go beyond the approximations made in "standard" modified continuum models used in the literature in terms of obtaining a more refined description of the local energy landscape.

To do so, our starting point is to derive a "local" TB Hamiltonian, $\hat{H}^{local}$, that can be diagonalized at each lattice site. In a first step, a supercell of, for instance, an (In,Ga)N/GaN QW is generated, which may contain the relaxed atomic positions. Based on this supercell, the corresponding TB Hamiltonian is generated. Diagonalizing this full TB Hamiltonian would give the single-particle states and energies. However, to obtain the local band edges and, thus, an energy landscape $V(\mathbf{r})$, at each lattice site a *local* TB Hamiltonian, $\hat{H}^{local}$, which in the case of our nearest neighbor sp^3 TB model is a 8×8 matrix, is constructed from the full TB Hamiltonian. $\hat{H}^{local}$ now describes the local environment of the atom at a given site and takes the form

$$\hat{H}^{local} = \begin{pmatrix} E^0 & H_{int}^{1-4} \\ H_{int}^{1-4\dagger} & E^{1-4} \end{pmatrix}. \tag{2}$$

Here, E^0 is a 4×4 matrix describing the on-site energies of s, p_x, p_y, and p_z orbitals of the lattice site at which the energy landscape will be calculated. The 4×4 matrix H_{int}^{1-4} describes the interactions (hopping matrix elements) between orbitals at the lattice site under consideration and the orbitals at its four nearest neighbors. Finally, the 4×4 matrix E^{1-4} contains the average on-site energies for s and p-orbitals of the nearest neighbors of the atom at which the local band edge is calculated. Given that these matrix elements of $\hat{H}^{local}$ are directly taken from the full TB Hamiltonian, the effects of (local) strain and built-in polarization fields are *a priori* included in the local band edges. Once this energy landscape is obtained, it is transferred to a regular wurtzite grid and passed to a continuum-based solver to obtain the electronic structure or perform transport calculations; it is not necessary to calculate strain and built-in fields in the continuum-based model. In this manner and as already stressed above, we circumvent the demand for any averaging to find the "local" In composition and then to calculate averages of elastic or piezoelectric constants to obtain these fields. Again, any bowing of valence or conduction band edges seen in atomistic calculations of, e.g., III-N alloys,[38] are directly encoded in the local TB band edges and should be transferred to the continuum model. We note three important aspects of the procedure. First, given that we are using a nearest neighbor TB model, the interactions in the above local TB Hamiltonian are restricted to nearest neighbors to correctly reproduce the local band edges of, for instance, an unstrained bulk system; the full TB Hamiltonian includes only interaction matrix elements between nearest neighbor anions and cations but not second-nearest neighbor cation–cation or anion–anion hopping matrix elements. If a second-nearest neighbor TB model is used, then interactions up to second-nearest neighbor would have to be included in the local Hamiltonian to obtain a correct description of even the unstrained bulk band edges. Second, the approach can be used for any strain dependent TB Hamiltonian, even if the atoms are displaced from the ideal bulk positions, given that the local band edges are determined from the matrix elements of the full TB Hamiltonian which depend on the relative position of the atoms (and the corresponding strain corrections). The only prerequisite is that local band edge energies are placed on a grid that is appropriate for the desired continuum-based modeling. Finally, we note that there are different ways of calculating the local band edges. In the following, we have evaluated the local band edges at both anion and cation sites to achieve a higher resolution of the landscape. However, alternative approaches could calculate the band edge energy only at either the anion or cation sites. Future studies may now look at these alternative schemes, while in the following we use the full anion cation structure.

An example of the local conduction band edge (CBE) and valence band edge (VBE) calculated from the TB method via the local TB Hamiltonian for a simple VCA-type system in the absence of strain and built-in fields is shown in Fig. 2 (open circle, $E_{TB}^{CBE/VBE}$) for a linescan along the wurtzite c-axis. Here, we use a 2.6 nm wide $In_{0.15}Ga_{0.85}N$ QW; the cell size is approximately $10 \times 9 \times 15\,nm^3$. We note that the band edges obtained reveal a slightly softened QW interface, which arises from the fact that at the interface between

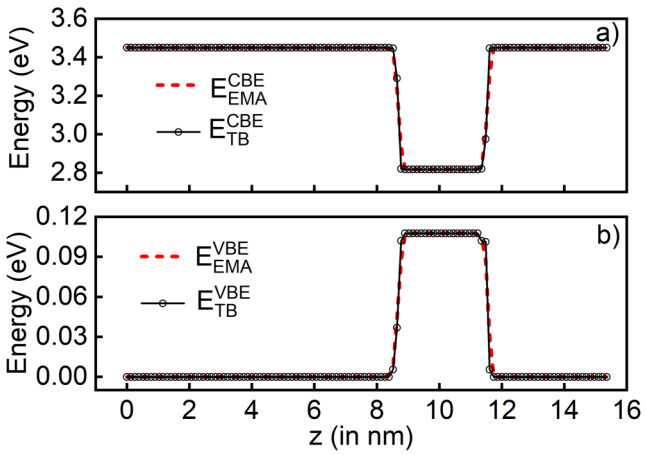

FIG. 2. Linescan of the potential energy profile in a (In,Ga)N/GaN quantum well with 15% In along the wurtzite c-axis. The system is treated within a virtual crystal approximation (VCA) without strain and built-in fields. The TB data is given by the black open circles, while the FEM mesh data using the TB data as input is shown by the red dashed line. (a) Conduction band edge (CBE); (b) Valence band edge (VBE).

© Author(s) 2021

GaN and (In,Ga)N N-atoms are exposed to varying numbers of Ga and virtual InGa atoms.

Regarding the computational costs of this approach, we note that for determining the local band edges, the full TB Hamiltonian only needs to be stored in the memory but does *not* need to be diagonalized. For the local band edge calculations, only 8×8 matrices need to be diagonalized, which may even be distributed between different cores if needed in future studies. Finally, our VFF model is implemented in LAMMPS which is designed to run on a large number of CPUs.[44] We have recently relaxed (In,Ga)N/GaN QD systems with $> 1\,000\,000$ atoms, using the same the VFF model applied here.[45] In the literature, VFF models underlying QD calculations have efficiently relaxed structures with $> 50\,000\,000$ atoms.[46] Thus, overall when optimizing our approach further, large scale calculations with several million atoms will be within reach of this method in a numerically efficient manner.

B. Connecting atomistic and continuum-based grid: Atomistic FEM mesh generation

Having described the TB model and how the local band edges can be obtained from such a theory, we address in this section how this information is transferred to a finite element method (FEM) mesh, which can then be used for continuum-based calculations. Given that the TB energy landscape is known at each lattice site in the TB supercell, we generate a so-called *atomistic FEM mesh* that has as many nodes as atoms in the system; the atomistic FEM mesh is generated using WIAS-pdelib and TetGen,[47] see Figs. 3(a) and 3(b). Figure 4 depicts an example mesh for a TB model when applying a VCA. In this test system, the structure has 126 780 atoms and the corresponding TetGen generated mesh has 126 780 nodes and 891 188 tetrahedra. We note that the interface between the (In,Ga)N QW and GaN barrier region is again not sharp. As discussed already above, this is attributed to the atomistic effect that the local environment of a N-atom at the well barrier interface "sees" a varying number of Ga and in this case virtual InGa atoms, which now is also transferred into our atomistic FEM mesh and will also come into play when dealing with random alloys.

The established atomistic FEM mesh can now be used to generate input for continuum-based models, including single- or multi-band $\mathbf{k} \cdot \mathbf{p}$ approaches[25,30,33] as well as a localization landscape theory description.[18,48] Using the WIAS-pdelib software again, the data from the atomistic FEM mesh are transferred to a 3D equidistant uniform tensor-product point-set that is compatible with the plane waves based code SPHInX by interpolation, see Fig. 3(c). Generally, we define a point p_0 and (n_1, n_2, n_3) subdivisions in all the three directions (x, y, z) to overlay $n_1 \times n_2 \times n_3$ points on a part of the FEM mesh. Usually, we want not to cover the entire FEM mesh whereas the points outside will be ignored by SPHInX. To transfer the data, we generate a tensor mesh from the $n_1 \times n_2 \times n_3$ points with same number of points and then using linear mesh to mesh interpolation. The tensor mesh is necessary to use the point-neighborhood information for local efficient tensor-point to FEM-cell searching. On simpler terms, we overlay a subdomain of the FEM mesh with points and linear interpolate the data from the FEM mesh to this points for SPHInX. The points are arranged in cuboid with axes (x, y, z) with (n_1, n_2, n_3) subdivisions.

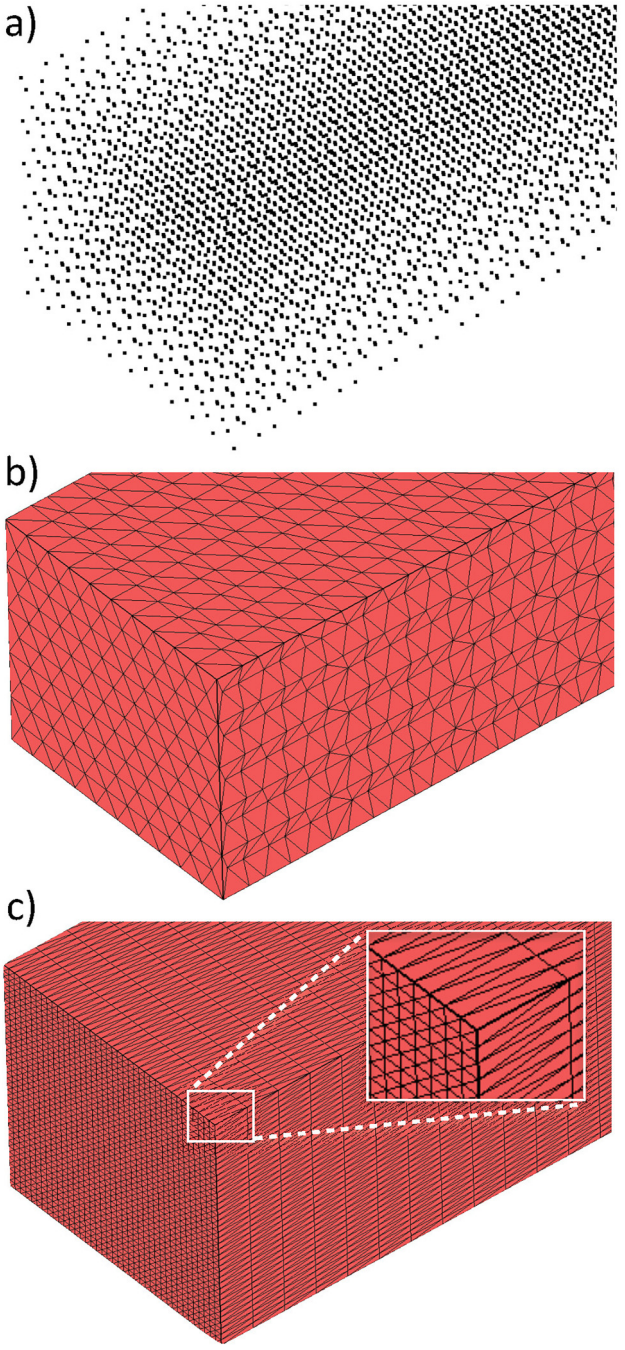

FIG. 3. Transformation of the tight-binding lattice to a FEM mesh and ultimately to a SPHInX compatible input point-set. We start with a point-set (a) defined by the atomistic lattice positions as given by tight-binding. Using TetGen a tetrahedral mesh (b) is generated, which has exactly the same number of nodes as atoms in (a). In doing so, the tight-binding input is exactly represented on the nodes of the atomistic FEM mesh. The data from the atomistic FEM mesh are then transferred to a 3D equidistant uniform tensor-product point-set (c) compatible with the plane waves based code SPHInX by interpolation.

© Author(s) 2021

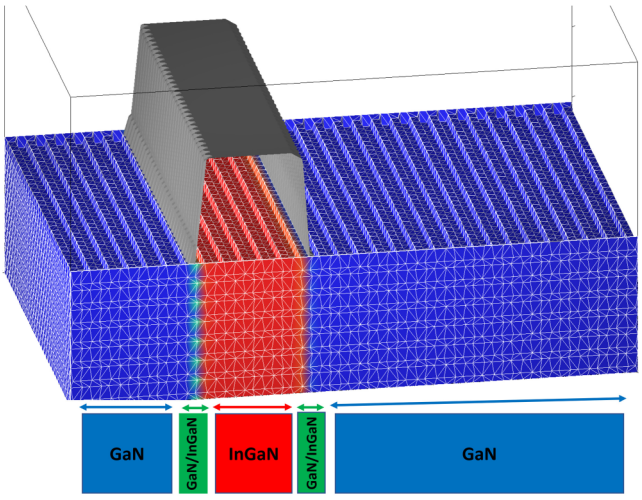

FIG. 4. Atomistic finite element mesh using the tight-binding energy landscape for a *c*-plane (In,Ga)N/GaN quantum well with 15% In in the well in a virtual crystal approximation; the valence band edge profile is given in gray. Material domains and interface regions are indicated in the lower part of the figure.

To demonstrate that the underlying TB data is transferred successfully into the FEM mesh and finally the mesh used for the continuum-based electron structure calculations, Fig. 2 shows (a) the CBE profile and (b) the VBE profile for a linescan along the *c*-axis of the 2.6 nm wide $In_{0.15}Ga_{0.85}N$ QW (already mentioned in Sec. II A). The TB band profile is given by the black solid line while the red dashed line is the mesh generated for the SPHInX calculations. As expected and required, the SPHInX compatible mesh reproduces the TB landscape. Having established a connection between the TB energy landscape and the mesh used in our EMA calculations, we discuss how these data are now processed in the continuum picture within the SPHInX library.

C. Continuum-based model

The backbone of our continuum-based EMA calculations is the plane wave based software library SPHInX.[49,50] This highly flexible package facilitates, in general, the three-dimensional calculation of strain and polarization fields as well as the electronic structure of semiconductor nanostructures. Here, arbitrary stiffness and piezoelectric tensors as well as multi-band $\mathbf{k}\cdot\mathbf{p}$ Hamiltonians can be defined without any recoding.[32] All these quantities can be defined in an input file in a human-readable meta-language.

Given that the confining TB energy landscape contained is already known on a continuum-based grid, only the kinetic part of the Hamiltonian has to be provided. In what follows, we apply a single-band EMA for several reasons. First, it is a simple approach with just one adjustable parameter (the effective mass) that will allow a systematic method development study. Multi-band models, while we discuss and comment throughout the paper on their potential benefits, which would account for effects such as conduction band valence band coupling or valence band mixing, are beyond the scope of the present work. A multi-band study would increase number of free and adjustable parameters significantly (A_i—valence band parameters; Kane parameters; etc.),[51,52] not to mention their composition dependence or the still large degree of uncertainty in these parameters in the literature;[51] all this would further complicate the comparison between continuum and atomistic results. Additionally, one needs to bear in mind that single-band effective mass models are widely applied in the literature when describing carrier localization effects in InGaN QWs. Thus, focusing on single-band effective mass models in comparison with an atomistic model allows us to flesh out potential problems with a one-band model in general.

However, we also stress again that given the flexibility of the framework, follow-up studies can be easily extended to six- or eight-band $\mathbf{k}\cdot\mathbf{p}$ models,[25,53] which may be targeted in future studies. We remind again that the TB energy landscape already contains (local) strain and built-in fields so that these quantities do not have to be calculated within the continuum model. However, the computational burden will increase significantly if the atomistic FEM mesh is used in combination with a multi-band $\mathbf{k}\cdot\mathbf{p}$ model in comparison to a single-band EMA. In fact for a multi-band $\mathbf{k}\cdot\mathbf{p}$ model, the computational burden may be similar to the TB modeling on the *active region* of a full device structure. But, even the multi-band $\mathbf{k}\cdot\mathbf{p}$ model has a distinct advantage over the atomistic TB model, namely, that in such a continuum-based model the meshing in different spatial regions can be adjusted. This is in contrast to the TB framework where one is bound to the atomistic resolution. Thus, in the TB benchmarked continuum-based model, one may use the atomistic resolution in the active region but a coarser grained mesh in, for instance, the *n*- and *p*-doped regions of a device. We have already presented initial results for drift-diffusion calculations of an InGaN QW-based device.[54]

In terms of the material parameters and the fact that we are using a single-band EMA, only the electron and hole effective masses have to be defined. In the following, we will use a constant effective mass throughout the whole simulation cell that will be adjusted by the average alloy content in the well. How these masses and their composition dependence are determined will be discussed in more detail below.

Overall, we highlight again that the proposed framework is different from previous studies in the literature, given that we are directly transferring an TB derived energy landscape into the continuum-based solver. Thus, in our case and given that we are using a single-band EMA, basically the only free input parameters in the continuum-based model are the effective masses. Furthermore, this approach now allows for direct comparison of the results of EMA and the TB model on the same alloy configuration (VCA and microscopic random alloy); such a comparison will be discussed in Secs. III and IV.

III. RESULTS

In this section, we present the findings on the electronic structure of $In_xGa_{1-x}N$ single QWs obtained within TB and continuum-based calculations. To study the impact of the In content on the results, values of 5%, 10%, 15%, and 25% In are considered in the following. Before turning to the random alloy analysis, we start

© Author(s) 2021

with VCA calculations in Sec. III A. Given that the continuum-based calculations in this first, single-band approach contain only two free parameters, namely, the effective electron and hole masses, we use the VCA model system to analyze and calibrate the single-band EMA in general. The calibrated model is then used for analyzing the impact of random alloy fluctuations on the electronic structure of (In,Ga)N QWs, and the results of these studies are presented in Sec. III B.

A. VCA comparison

In this section, we present the outcome of our VCA studies. As already mentioned above, the aim is to calibrate the EMA against the TB data. While a very good agreement between TB and effective mass model is in general expected, a calibration step is essential for several reasons. First, without establishing very good agreement between the EMA and TB model for a simple VCA case, it will not be clear if any potential differences between the two methods (in the random alloy case) stem entirely from the alloy fluctuations or are "pre-existing differences" which may originate from the difference in the predicted/used effective masses in the two models. The VCA comparison helps to eliminate such "pre-existing differences." Second, given that bulk effective masses are in general input parameters in any continuum-based model, we use calculations in the absence of strain and built-in fields to potentially adjust the effective masses employed in our EMA model to reproduce the TB data. Performing such an analysis as a function of the In content x in the well allows us to establish a composition-dependent effective mass, which can then be used in calculations accounting for random alloy fluctuations. Since we are interested in establishing the general framework, a position *independent* effective mass is applied, meaning that the effective mass in the well and in the barrier are identical. Here, several refinements are possible, e.g., having a position dependent effective mass, performing calculations in the presence of strain and built-in field so that the effective mass contains corrections arising from these effects. However, the latter are usually not taken into account in standard approaches dealing with (In,Ga)N/GaN QWs in a continuum-based framework. It is important to note that above ansatz of a strain independent effective mass is similar to previous works in the literature.[55,56] However, it differs from those studies by how the local band edges are treated. For instance, in the advanced continuum model of Ref. 57, the effective masses in an EMA were also treated as strain independent. However, to achieve an excellent agreement between an EMA and an atomistic TB, nonlinear strain corrections were included in the EMA. It is important to note that EMA and atomistic TB model were treated independently in Ref. 57, which means that the strain effects in the local band edges are calculated separately in the continuum model and in the atomistic model. In our framework, this is different since it is not necessary to calculate the strain effects in the EMA model separately, they are build into the local band edges obtained from TB directly. This highlights again the benefit of our presented framework in comparison to previous literature work. Therefore, our starting point for obtaining the effective masses of $In_xGa_{1-x}N$ as a function of x, is a linear, composition weighted interpolation of the electron and hole masses for wurtzite InN and GaN via $m^{e,h}_{In_xGa(1-x)N} = x m^{e,h}_{InN} + (1-x) m^{e,h}_{GaN}$.

Here, m^e are the electron and m^h are the hole masses, taken from Ref. 52, using equations in Ref. 58 for determining the hole masses. For all calculations, we use as a test system a 2.6 nm wide $In_xGa_{1-x}N$/GaN single QW. The simulation cell is approximately $10 \times 9 \times 15\,nm^3$. The cell contains 126 780 atoms. The tensor-product mesh underlying all SPHInX-based EMA calculations uses a grid with a uniform step size of 0.2 nm, resulting in $50 \times 44 \times 77$ grid points.

Figure 5(a) depicts the energies of the electron ground ($E_0^{e,\alpha}$) and first two excited states ($E_{1,2}^{e,\alpha}$) as a function of the In content x in the well obtained within EMA (α = EMA) and TB (α = TBM). As Fig. 5(a) shows, already when using the effective mass parameters from Ref. 52 and the linear, composition weighted interpolation scheme for the effective mass we find a very good agreement

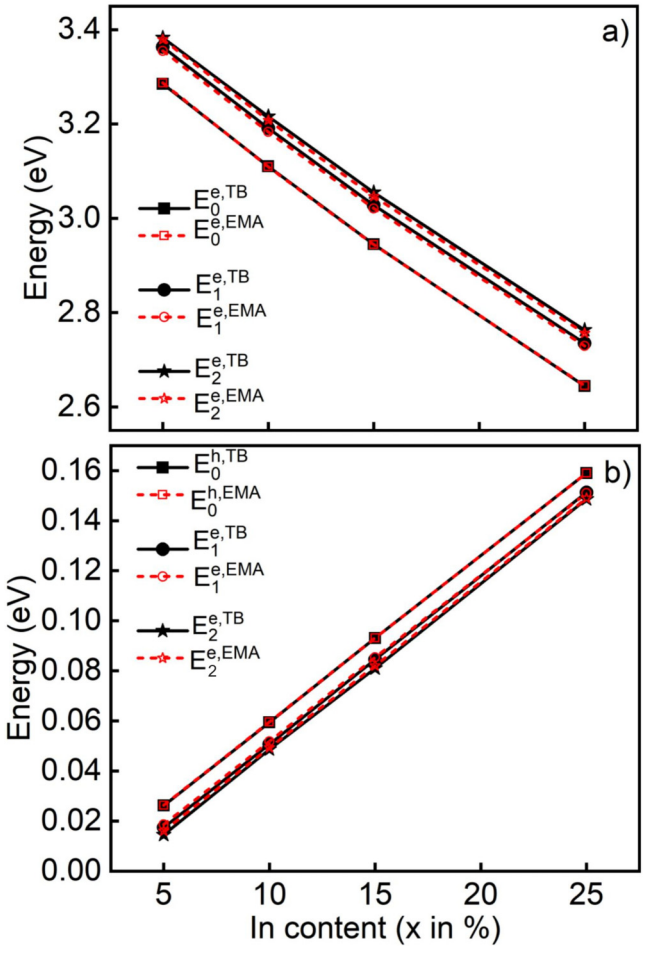

FIG. 5. (a) Electron and (b) hole single-particle ground and first two excited states for a 2.6 nm wide $In_xGa_{1-x}N$/GaN quantum well in virtual crystal approximation and in the absence of strain and built-in fields. The results are shown as a function of the In content x.

© Author(s) 2021

between EMA and the TB model. This is not only true for the ground state energies but also for the excited states.

Turning to the hole energies $E_i^{h,\alpha}$ (where i=0 denotes the ground state whereas i=1,2 are the first, second excited state), depicted in Fig. 5(b), we find also a very good agreement between EMA ($E_i^{h,EMA}$) and TB ($E_i^{h,TBM}$) results. We note that when neglecting spin–orbit coupling effects, the hole ground state is twofold degenerate in the TB model. However, given its single-band character, this effect is not captured in the EMA and would, therefore, require a multi-band model. Given the flexibility of our underlying SPHInX framework such an extension on the continuum-based modeling can be implemented in a straightforward way. However, for the current work, we are mainly interested in the impact of random alloy fluctuations on the electronic structure of (In,Ga)N QWs, for which also in the literature single-band approaches have been used, and we do not apply a two- or six-band model here.

Given the good agreement between EMA and TB for electron and hole ground state energies also the ground state transition energies, $\Delta E^{\alpha}(x) = E_0^{e,\alpha}(x) - E_0^{h,\alpha}(x)$, are in very good agreement over the full composition range considered. The calculated values differ by no more than 2 meV. Equipped with this calibrated EMA model, we present the results of calculations which account for random alloy fluctuations in Sec. III B.

B. Random alloy case: Single-particle energies

In this section, we compare the results from the calibrated EMA model with TB data for c-plane (In,Ga)N/GaN QWs in which random alloy fluctuations are considered in the well region. Again these calculations have been performed as a function of the In content in the well; we consider here the same In content range as in the VCA calculations, namely, 5%, 10%, 15%, and 25% and use the (In,Ga)N/GaN QW structures studied in Ref. 9. For these systems, the TB model has shown to give good agreement with experimental data in terms of photoluminescence peak energies and full width at half maximum values.[35] The simulation cell is approximately $10 \times 9 \times 10\,\mathrm{nm}^3$ and contains 819 20 atoms. For each In content, ten different random alloy configurations have been generated, allowing us to study the impact of the alloy microstructure on the results. To avoid any preferential orientation or correlation of In atoms, we proceed as following. In the first step, we attribute to each cation site a random number. Then, in a second step, the number of cation sites, n, that have to be occupied by In atoms on the grid to reflect the desired In content x is determined. In the final step, the n lowest random numbers at the cation sites of the mesh are selected as In atoms while the remaining cations sites are Ga atoms. Using this procedure, in the following, we look at results averaged over the ten different microscopic configurations per In content. In the continuum-based calculations, we keep the grid spacing consistent with our calibrated VCA model, thus, the underlying SPHInX-based EMA calculations use a tensor-product mesh with a uniform step size of 0.2 nm, resulting in $50 \times 44 \times 50$ grid points.

1. Electron single-particle energies

Figure 6 shows the electron energies of the ground and first nine excited states for (a) 5%, (b) 10%, (c) 15%, and (d) 25% In.

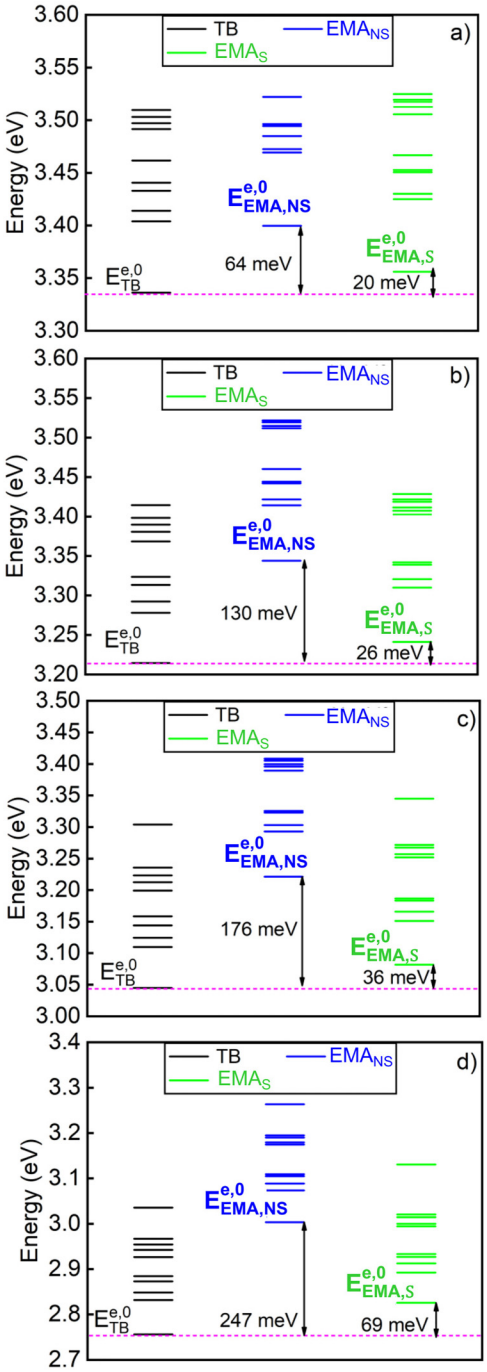

FIG. 6. Energies of the energetically lowest ten electron states in c-plane (In,Ga)N/GaN quantum wells with In contents of (a) 5%, (b) 10%, (c) 15%, and (d) 25%. The results are averaged over ten different random alloy configurations. The data are shown for the TB model (solid black line), the single-band EMA without shift (solid blue line) and with shift (solid green line) of the band edges; more details are given in the main text. The ground states are marked as $E_{TB}^{e,0}$ for TB, $E_{EMA,NS}^{e,0}$ for EMA without shift, and $E_{EMA,S}^{e,0}$ for EMA with shift.

© Author(s) 2021

The data are always averaged over the ten microscopic configurations considered. The TB data are given in black together with two sets of EMA results (green and blue), which will be explained below. We first focus on the EMA results given in blue and denoted by "No shift", abbreviated as NS in all the panels of Fig. 6. This calculation corresponds to the situation where the TB energy landscape is directly used in the EMA calculations and the electron and later hole effective mass for the corresponding In content are chosen based on the VCA results discussed above. From Fig. 6, several important aspects can be inferred. The most striking difference between TB and EMA results (No Shift) is that the ground state energies $E^{e,0}_{TB}$ and $E^{e,0}_{EMA,NS}$ differ significantly; this difference increases with increasing In content. However, while there is a larger difference between ground state energies, the energetic separation, $\Delta E^{GS,\,EX}_{\alpha} = E^{e,1}_{\alpha} - E^{e,0}_{\alpha}$, of the ground state $E^{e,0}_{\alpha}$ and the first excited state between the two models differs, independent of the In content, by less then 4 meV. Note, in the expression $\Delta E^{GS,\,EX}_{\alpha}$, the superscript "GS" refers to the ground state, whereas the superscript "EX" refers to the excited states under consideration. Thus, while one may be tempted to increase the effective electron mass to obtain a better agreement between TB and EMA (No shift) ground state energies, such an increase in the mass will affect (reduce) the energetic separation between excited states in the EMA. Additionally, given that the electron energies in the case of the EMA are shifted to higher energies when compared to the TB results, one may expect an earlier onset of carriers becoming more delocalized and, thus, may alter the description of carrier localization effects due to random alloy fluctuations. All these (energetic separation of states; earlier onset of delocalization) are, however, important when studying quantities such as the radiative recombination rate with increasing temperature or carrier density in *c*-plane (In,Ga)N/GaN systems, where the density of excited states plays an important role.[24,59] Based on all this, and even though the EMA labeled "No Shift" operates on the same energy landscape as the TB model, it gives energy eigenvalues that on an absolute scale are very different from the TB model.

The above seen deviation between TB and EMA exposes shortcomings of the single-band continuum model. The agreement between the continuum and the atomistic model may be improved by moving to a multi-band band approach on the continuum model side since aspects such as band nonparabolities would be captured. However, our aim in the current study is to establish (i) a general framework that allows us to bridge the gap between continuum-based calculations and atomistic models and (ii) an EMA model that operates on the energy landscape obtained from the TB model with a minimum number of free and adjustable parameters while at the same time facilitating a good approximation of the TB results. It has already been highlighted by Auf der Maur *et al.*[13] that quantities such as the bandgap evolution in a VCA-type approximation may give a very different result as compared to an atomistic calculation that includes alloy fluctuations. In such a case, the bandgap bowing parameter may be adjusted (increased) to correct this. Here, we follow a similar approach to achieve a simple effective mass model that provides a good description of the TB results and adjust the band offset in the QW region by a rigid, constant energy shift ΔE^{S}_{CBO} (conduction band) and ΔE^{S}_{VBO} (valence band); all calculations have been repeated with the adjusted band offsets for electrons and holes. The results are shown in Fig. 6 in green and are labeled by "EMA_S." The applied ΔE^{S}_{CBO} (conduction band) and ΔE^{S}_{VBO} (valence band) shifts in the EMA model to the TB energy landscape in the QW region are summarized in Fig. 7 along with a quadratic fit of the form $\Delta E^{S,f}_{\alpha}(x) = ax + bx^2$; the extracted coefficients *a* and *b* are also given in Fig. 7; bowing parameters for the band offsets are not unusual in III-N-based materials as shown in the literature.[38,40,60] Here, we have obtained ΔE^{S}_{CBO} from the average electron ground energy difference in the TB and the EMA_{NS} (No Shift) models, cf. Fig. 6. Applying this rigid shift to the band edges within the well and repeating the calculations results in a much better agreement between EMA_S (green solid lines) and TB ground and excited state energies. For instance, in the 25% In content case, cf. Fig. 6(d), the difference between the TB ground state energy, $E^{e,0}_{TB}$, and the ground state energy in EMA without applying the shift, $E^{e,0}_{EMA,NS}$, is 247 meV. Looking at the ground state energy when ΔE^{S}_{CBO} is applied, $E^{e,0}_{EMA,S}$, we find a difference of only 69 meV with respect to the TB model. Also, the energetic separation between the ground and the first excited state is similar. For the TB model, we obtain $\Delta E^{GS,EX}_{TB} = 72$ meV and for $\Delta E^{GS,EX}_{EMA,S} = 68$ meV. We note that especially at higher In contents (> 15% In), the deviations between the two models become larger when compared to the lower contents, even with the shift applied. But, as we will discuss below, on the energy scale of the transition energies, these deviations are of secondary importance.

The additional benefit of applying ΔE^{S}_{CBO} is that the energy range over which the first ten electron states found is very similar between TB and EMA_S. Thus, at least in terms of the energy eigenvalues, the modified EMA with an energetic correction to the CB edge presents an attractive model to describe the electronic structure of (In,Ga)N/GaN with random alloy fluctuations in the well to achieve a reasonable approximation of the atomistic data on average without increasing the numerical effort of the model.

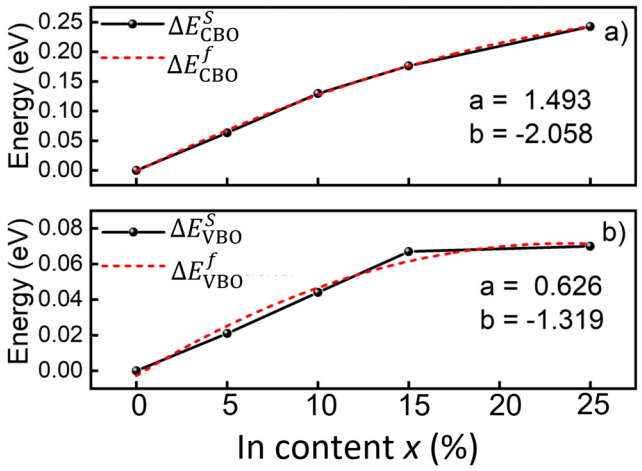

FIG. 7. Band offset correction for (a) conduction and (b) valence band edge as a function of the In content *x*. The data are fitted with the equation $\Delta E^{S,f}_{\alpha}(x) = ax + bx^2$. The obtained *a* and *b* values are given in (a) and (b) for the conduction $[\Delta E^{S,f}_{CBO}(x)]$ and valence bands $[\Delta E^{S,f}_{VBO}(x)]$, respectively.

© Author(s) 2021

Additionally, having established the bowing parameters for the energy offset as a function of the alloy content allows us to apply the model in future studies with different In contents or larger systems without the need to perform a full TB calculation. As already discussed in Sec. II A, only the energy landscape needs to be extracted from the full TB Hamiltonian, which requires only storing of the full Hamiltonian but not diagonalizing it; only 8×8 sub-matrices are required to be diagonalized.

2. Hole single-particle energies

Next, we turn our attention to the energies of the first ten hole states. The results from the three different models, discussed above for electrons, are shown in Fig. 8 for hole state energies in *c*-plane (In,Ga)N QWs with (a) 5%, (b) 10%, (c) 15%, and (d) 25% In content. The data displayed in the figure are again averaged over the ten different microscopic configurations. The solid horizontal black lines denote the TB results, while the blue and green lines give the results from the modified EMA models without and with applying a shift ΔE^{S}_{VBO} to the VBE in the well. Figure 8 reveals that without shifting the VBE in the well region, the EMA_{NS} (blue) noticeable underestimates the ground state energy; in general, this difference increases with increasing In content [cf. Figs. 8(a)–8(d)]. Furthermore, without shifting the VBE in the EMA, the energetic separation between the ground and first excited state is, in general, smaller when compared to the TB results. For instance, in the 10% In case, cf. Fig. 8(b), in TB, this energetic separation is $\Delta E^{h,GS,EX}_{TB} = E^{h,0}_{TB} - E^{h,1}_{TB} \approx 22$ meV, while in the modified EMA_{NS} one finds $\Delta E^{h,GS,EX}_{EMA,NS} = E^{h,0}_{EMA,NS} - E^{h,1}_{EMA,NS} \approx 9$ meV. This could indicate that carrier localization effects, especially for states close to the VBE, are not well described in EMA_{NS}. Thus, the wave functions calculated using EMA_{NS} may exhibit a more delocalized nature when compared to the TB wave functions. We will come back to this question further below when discussing the inverse participation ratio (IPR) values of the different states.

All this again highlights the shortcomings of the single-band EMA which may be cured in part by applying a multi-band model. However, instead of targeting the problem with the computationally heavier multi-band model, we follow the procedure applied for the electrons and construct a modified EMA, EMA_S, which includes a shift of the VBE in the QW region. As one can infer from Fig. 8, this model gives energies that are in reasonable agreement with the TB energies. The respective shifts are displayed in Fig. 7(b); the data are fitted by $\Delta E^{S,f}_{VB} = ax + bx^2$, where and a and b are given in the figure. With these shifts applied, differences in ground state energies between TB and EMA_S are below 10 meV in the 5% [cf. Fig. 8(a)], 10% [cf. Fig. 8(b)], and 25% [cf. Fig. 8(d)] In cases. Only for 15% we find a slightly larger difference between TB and EMA_S of approximately 19 meV [cf. Fig. 8(c)]. However, this difference is significantly reduced compared to the 68 meV difference between TB and EMA_{NS} and further refinements can be made by adjusting the VBE shift further. However, to demonstrate the general strategy of our modified EMA, the achieved agreement between TB and EMA_S is sufficient for our purpose. But, we note also that while the agreement between the ground state energies is improved, the energetic separation between excited states may not be improved in general. Looking again at the 10% In case, Fig. 8(b),

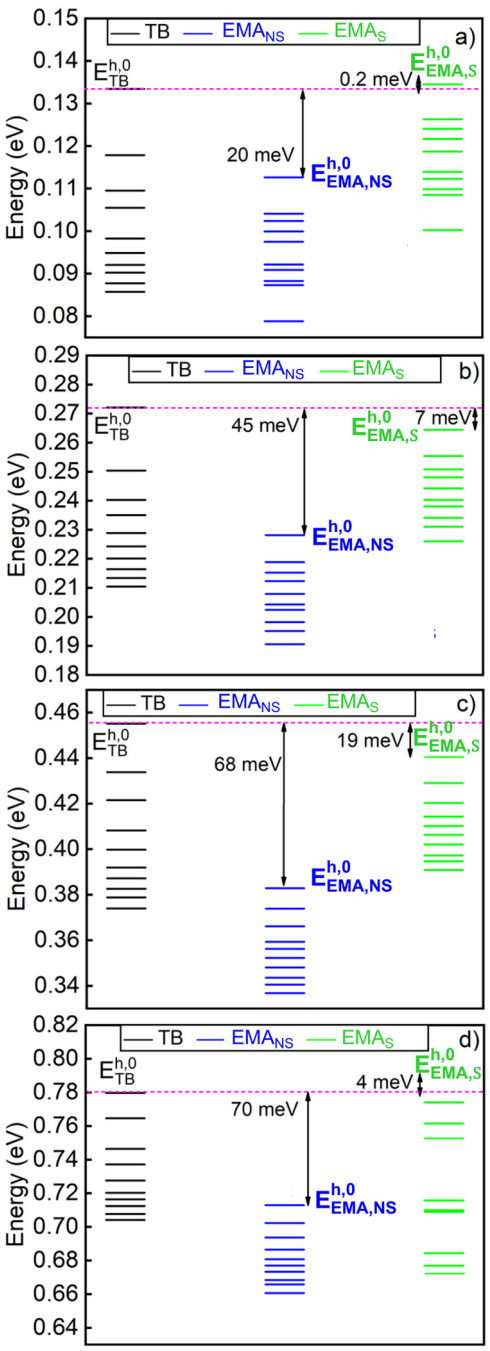

FIG. 8. Energies of the first ten hole states closest to the valence band edge in (In,Ga)N/GaN *c*-plane quantum wells with In contents of (a) 5% , (b) 10%, (c) 15%, and (d) 25% In. The data are averaged over ten different random alloy configurations. The results are shown for the TB model (solid black line), the single-band EMA without (solid blue line) and with shift (solid green line) of the band edges; more details are given in the main text. The ground states are marked as $E^{e,0}_{TB}$ for TB, $E^{e,0}_{EMA,NS}$ for EMA without shift, and $E^{e,0}_{EMA,S}$ for EMA with shift.

© Author(s) 2021

in TB we find $\Delta E_{TB}^{h,GS,EX} \approx 22$ meV, while in the modified EMA_S, the separation is $\Delta E_{EMA,S}^{h,GS,EX} = E_{EMA,S}^{h,0} - E_{EMA,S}^{h,1} \approx 10$ meV.

Finally, we briefly discuss the average ground state transition energy, $\Delta E_\alpha^0 = E_\alpha^{e,0} - E_\alpha^{h,0}$, which is displayed in Fig. 9 as a function of the In content for the three different methods (α = TB, EMA_S, EMA_{NS}). Overall, the graph shows the expected behavior that with increasing In content x the transition energy shifts to lower energies, given the increase in built-in field and reduction in the bandgap of an (In,Ga)N alloy in general with increasing In content. Also, as expected from our discussion above on the electron and hole ground state energies, compared to the TB transition energy (black squares), the EMA without the energetic shift to the band edges, EMA_{NS} (blue circles), significantly overestimates the bandgap energy; this difference is more pronounced for higher In contents. On the other hand, the EMA model that includes the shift in the band edges, EMA_S (green triangles), gives a very good description of the transition energy over the full composition range, inline with our analysis of the ground state energies above. Finally, we show the standard deviation (σ_α) of the distributions of the transition energies as a function of the In content by color coded error bars in Fig. 9. The error bar marked in black represents σ_{TB}, the green denote $\sigma_{EMA,S}$ and the blue denote $\sigma_{EMA,NS}$. σ_α for each method is calculated by using the following formula:

$$\sigma_\alpha = \sqrt{\frac{\sum_i (\Delta E_{\alpha,i}^0 - \Delta E_\alpha^0)^2}{n}}, \tag{3}$$

where $\Delta E_{\alpha,i}^0$ is the transition energy corresponding to each configuration for the different methods, ΔE_α^0 is the average ground state transition energy, and n is the total number of configurations (ten for each In content). In general, we find that the standard deviation (σ_α) increases with the increase in In content. This is consistent for all the methods. For instance, σ_{TB} in the case for 5% and 15% In are 0.156 eV and 0.205 eV, respectively. Similarly, $\sigma_{EMA,S}$ for 5% and 15% In are 0.140 eV and 0.209 eV, respectively, whereas $\sigma_{EMA,NS}$ for the same In content are 0.143 eV and 0.178 eV, respectively.

Overall, the presented analysis exhibits shortcomings of the single-band EMA. However, instead of increasing the computational load by moving to multi-band $\mathbf{k}\cdot\mathbf{p}$ models, we have proposed a simple modification of the EMA approach to achieve a good agreement with the atomistic TB results over the In composition range of 5%–25%. Furthermore, having established a composition-dependent band edge adjustment parameter for the EMA allows us now to use this model in future calculations on the electronic and optical properties or for transport studies of (In,Ga)N QWs, without having to perform a full TB calculation.

Having discussed electron and hole energies, our analysis reveals that the developed modified continuum-based framework may give a good approximation of the TB data. However, as already mentioned above, wave function localization effects may be different. This aspect is, for instance, important for the wave function overlap, which impacts the (radiative) recombination rates.[6,24,59] In Sec. III C, we, therefore, focus our attention on wave function localization effects to further compare the outcome of modified EMA models with the TB data.

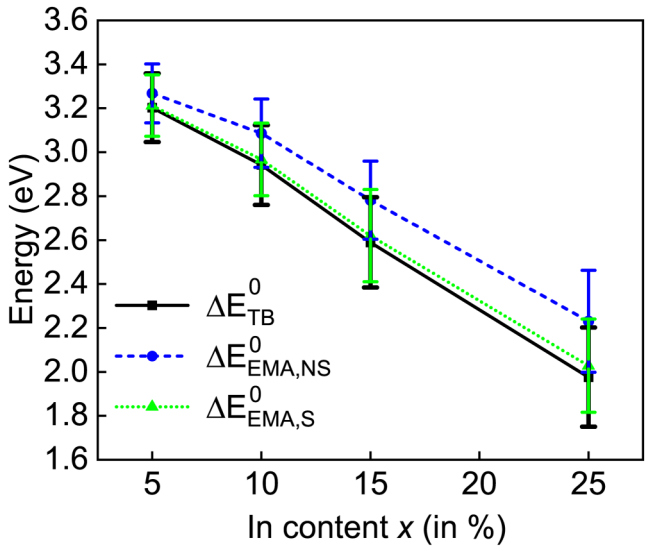

FIG. 9. Ground state transition energies in $In_xGa_{1-x}N$/GaN quantum wells as a function of the In content x. The black squares represent the tight-binding results (ΔE_{TB}^0), the green triangles give the results from the modified EMA with an energy shift applied ($\Delta E_{EMA,S}^0$), while the blue triangles denote the EMA results without an energy shift of the valence band edge in the well ($\Delta E_{EMA,NS}^0$). The data are averaged over ten different microscopic configurations per In content x. The standard deviation (σ) of the distributions of the transition energies for the three different methods are marked by the error bars colored in black (σ_{TB}), green ($\sigma_{EMA,S}$), and blue ($\sigma_{EMA,NS}$).

C. Random alloy case: Inverse participation ratio (IPR) for electrons and holes

In addition to comparing electron and hole energies, we also compare localization effects due to random alloy fluctuations. For the latter part, we employ the inverse participation ratio (IPR),[29,61,62] which provides a quantitative metric for this question. More details about the IPR value calculation, along with a detailed discussion why care must be taken when comparing IPR values obtained from atomistic and continuum-based models, are given in the Appendix.

In this subsection, we present the normalized IPR values ($\widetilde{IPR}$) for the ground and excited states obtained from TB and EMA (with and without shift). The results are averaged over ten different alloy configurations for each In content. For normalizing the IPR values, we proceed as follows. The TB electron ground state IPR value of the 5% In system represents our reference point. Thus, all TB IPR values are normalized with respect to this IPR value. Furthermore, we assume that for the 5% In case, the averaged electron ground state of the EMA including the energy shift, EMA_S, reflects the same carrier localization characteristics as the

© Author(s) 2021

averaged TB ground state for this In content. Thus also the IPR values of the EMA_S are normalized so that the average ground state IPR value of the 5% In system is also $\widetilde{IPR} = 1$. The obtained scaling factor to achieve this is applied to all EMA_S data and also the results of the effective mass model *without* the band edge shift, EMA_{NS}. If the localization features for the electron ground state are the same in EMA_S and EMA_{NS}, EMA_{NS} should also give $\widetilde{IPR} = 1$ for the system with 5% In. A more detailed discussion of this normalization procedure is given in the Appendix. In doing so, normalized IPR values, $\widetilde{IPR}$, provide also a more intuitive representation of the localization properties: if the $\widetilde{IPR}$ value exceeds a value of 1 it is more strongly localized than the electron ground state at 5% In in the well; a value below 1 indicates that the states are less localized when compared to the average electron ground state at 5% In. The $\widetilde{IPR}$ values for the first ten electron states are shown as a function of the state number in Fig. 10 for (a) 5%, (b) 10%, (c) 15%, and (d) 25% In.

Before looking at the individual In contents, Fig. 10 clearly shows that with increasing In content the (normalized) ground state $\widetilde{IPR}$ values predicted by all three methods increase. We attribute this to the fact that with increasing In content the piezoelectric field increases so that electron and hole wave functions localize at the opposing QW interfaces, in addition to localization effects due to random alloy fluctuations.

Turning now to the individual In contents and starting with the 5% In case, we find that the EMA model including the CBE shift (green triangles) both in terms of the magnitude of the $\widetilde{IPR}$ values and its evolution with state number reflects well the TB data (black squares). Also the model without the CBE shift (blue squares) gives a reasonable description of the average localization features of the TB model (black squares). However, with increasing In content, cf. Figs. 10(b)–10(d) deviations between TB and EMA models become more pronounced, especially for the energetically lower lying states. For higher lying states (state number > 5), especially EMA_S (including the CBE shift) describes these states very well; the EMA_{NS} (no shift) provides also a reasonable description but always gives lower values. We attribute the latter to the fact that the first ten electron states obtained within EMA_{NS}, as discussed in Sec. III B 1, cover on an absolute scale also a very different energy range when compared to the TB energy values; this may also affect the results. However, overall our presented analysis shows that the use of a rigid CBE shift within the well not only improves the agreement in energy levels between TB and EMA but also improves their average localization characteristics. Thus, the developed EMA should give on average a good approximation of the TB model.

Having discussed the electron $\widetilde{IPR}$ values above, we present these data now for the hole ground and excited states. We note that we are interested in studying the trends in localization characteristic by comparing the $\widetilde{IPR}$ values for different In contents and between different models. Looking at quantities such as carrier localization lengths for different In contents is beyond the scope of the present study but has been recently analyzed in the literature.[35] Figure 11 shows the average hole $\widetilde{IPR}$ values for (a) 5%, (b) 10%, (c) 15%, and (d) 25% In in the well. The data are again averaged over the ten different alloy configurations and are normalized with respect to the average electron ground state $\widetilde{IPR}$ value for 5% In (see above).

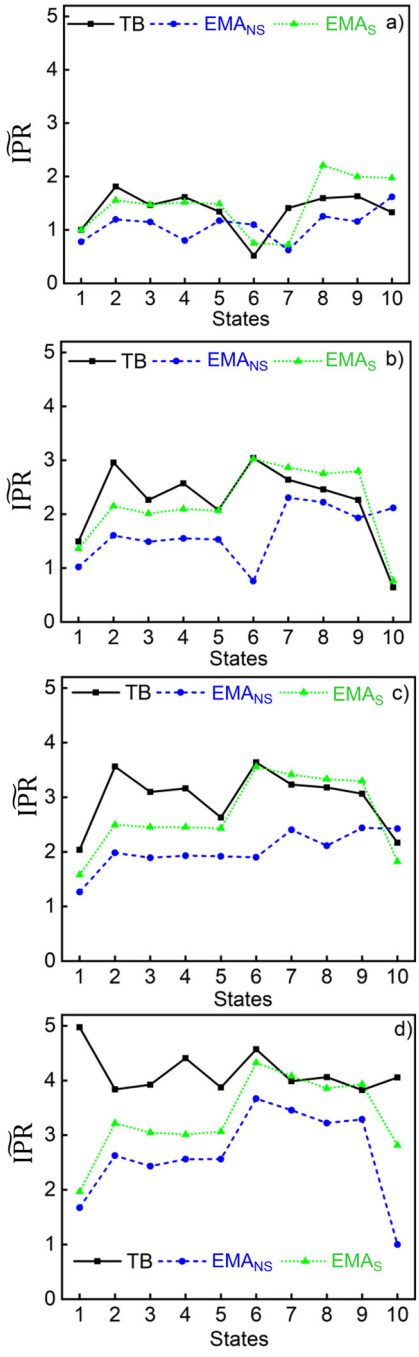

FIG. 10. Average normalized electron IPR values ($\widetilde{IPR}$) for *c*-plane (In,Ga)N/GaN quantum wells with varying In content: (a) 5% , b) 10%, (c) 15%, and (d) 25%. Black squares: tight-binding results; green triangles: single-band effective mass approximation in which the conduction band edge has been adjusted (see main text for more details); and blue circles: single-band effective mass approximation without the rigid conduction band edge shift. The data have been normalized to the average ground state electron IPR value of the 5% In case for tight-binding and shifted effective mass model, respectively.

© Author(s) 2021

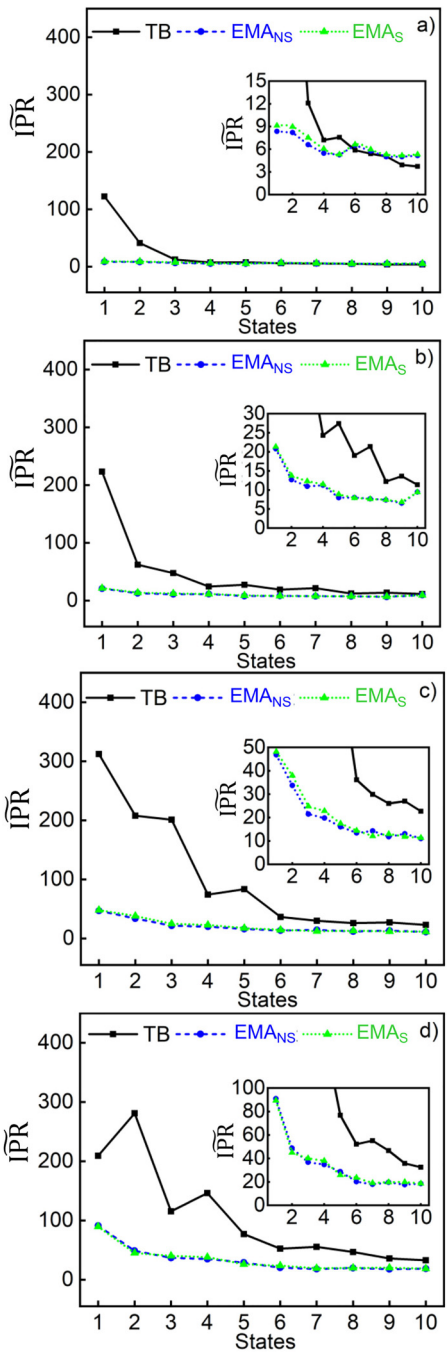

FIG. 11. Average normalized hole IPR values ($\widetilde{\text{IPR}}$) for *c*-plane (In,Ga)N/GaN quantum wells with varying In content: (a) 5%, (b) 10%, (c) 15%, and (d) 25%. Black squares: tight-binding results; green triangles: single-band effective mass approximation in which the valence band edge has been adjusted (see main text for more details); and blue circles: single-band effective mass approximation without the rigid valence band edge shift. The data have been normalized to the average electron ground state electron IPR values of the 5% In case for the tight-binding and shifted effective mass model (see Fig. 10).

Figure 11 reveals that the hole wave functions are far more strongly localized when compared to the electrons (see also figure insets and compare with Fig. 10). This finding is consistent with previous studies where charge densities of electron and hole wave functions have been inspected;[10,12,63] this effect is also captured by modified EMA models. However, and independent of the In content, the $\widetilde{\text{IPR}}$ values predicted by the EMA models are significantly smaller when compared to the TB model, at least for the states lying close to the VBE (energetically lowest lying hole states). For the ground states differences the EMA model (blue circles, green triangles) are smaller by a factor of order of 5–10. For higher lying states, the differences are less pronounced and similar to the electrons, a good agreement between the three different methods may eventually be achieved. It should be noted that here higher lying states refer to the states that are located deeper in the valence "band" and not the states that are significantly away from the Γ-point. Using the terminology of Ref. 7, by higher lying states we mean semi-localized states, where the impact of the alloy microstructure on the wave function localization is reduced and they approach the charge density distribution of a "standard" (no alloy fluctuations) QW.

Several conclusions can now be drawn from this. First, using a modified continuum-based approach to analyze and explain low temperature experimental results may be difficult since in this case the effects are dominated by states close to the VBE. These states may not be well captured in a modified single-band EMA. We note again that a better agreement may be expected when using a more sophisticated $\mathbf{k}\cdot\mathbf{p}$ model here. Second, while the modified EMA models describe the localization features of higher lying states better, studying the evolution of radiative recombination or Auger effects as a function of the temperature may also be difficult since the density of localized states may not be well captured. However, when dealing with higher temperatures and/or high carrier densities where now the physics are expected to be dominated by excited electron and hole states, the established modified continuum-based model should be in good agreement, in terms of energy eigenvalues and localization features, with the atomistic model. So using this model, e.g., in transport calculations at room temperature or beyond, our EMA_S should provide a good starting point without the need to perform these calculations in a fully atomistic framework.

IV. CONCLUSIONS

In this work, we have established a multiscale approach that allows us to connect atomistic tight-binding models with modified continuum-based methods. More specifically, we have developed an approach that extracts an energy landscape from an atomistic tight-binding model, including local variations in strain and built-in fields due to alloy fluctuations, on which single-band effective mass calculations have been performed to obtain the electronic structure of *c*-plane (In,Ga)N/GaN quantum well structures with different In contents. We stress that our developed ansatz goes beyond the widely used literature approach where the connection between atomistic and continuum-based theory is basically restricted to obtaining local alloy contents from an atomistic lattice that are used in continuum-based calculations. This local alloy information is often used to interpolate and

© Author(s) 2021

define basically bulk parameters, such as band offsets, on small local length scales, which in itself raises the question of validity of such an approach. With the model proposed here, we go beyond the local bulk parameter averaging by generating an energy landscape directly from tight-binding where the band edges are intrinsically modified by the presence of In and Ga atoms in the structure on a microscopic level. Furthermore, our framework is general and can be used for any tight-binding (sp^3, sp^3s^*, $sp^3d^5s^*$) and any continuum-based model (single- or multi-band). Finally, given that we have established an atomistic finite element mesh, it can also be extended beyond electronic structure calculations to transport simulations in the frame of drift-diffusion models.

Given the direct connection between atomistic tight-binding and single-band effective mass approximation in the sense that the calculations are performed on the same energy landscape, single-particle states and energies can directly be compared. We find that even when using such an energy landscape, significant differences in the single-particle energies are observed. However, our data also show that good agreement between a modified single-band effective mass approximation and tight-binding can be achieved for the first ten electron and hole state energies after applying a rigid shift to the band edges. This provides now a simple recipe for future studies, given that we have also determined the composition dependence of the rigid energy shift for electrons and holes. Overall, this allows us to use this further modified continuum model to achieve a good description of the single-particle energies in (In,Ga)N QWs without performing full TB calculations.

Turning to carrier localization effects, here studied via the inverse participation ratio, we find that even when shifting the band edges in the effective mass model, the continuum-based model underestimates the effects observed in the atomistic approach, especially for higher In contents (>15%); this effect is particularly pronounced for hole states. Thus, in situations where states near the conduction and valence band edge become important, for instance, at low temperatures or low carrier densities, the modified effective mass model may significantly underestimate the impact of carrier localization effects. This means also when studying quantities such as radiative or Auger recombination as a function of temperature or carrier density, care must be taken when drawing conclusions from a modified continuum-based approach. However, in the case where energetically higher lying states become important, the here established continuum-based model can give a very good approximation of the atomistic results. We also expect that a better agreement can be achieved by employing six- or eight-band $\mathbf{k}\cdot\mathbf{p}$ models rather than the single-band EMA used in the present work. Overall, the established model now presents an ideal starting point for further calculations on optical and transport properties of (In,Ga)N/GaN quantum well systems.

ACKNOWLEDGMENTS

The authors thank J. Fuhrmann (WIAS) for fruitful discussions. This work received funding by the Deutsche Forschungsgemeinschaft (DFG) under Germany's Excellence Strategy EXC2046: MATH+, project AA2-5 (O.M.), Sustainable Energy Authority of Ireland and Science Foundation Ireland (Nos. 17/CDA/4789 and 12/RC/2276 P2).

APPENDIX: INVERSE PARTICIPATION RATIOS

In this appendix, we discuss (i) general aspects of the IPR value calculation in atomistic and continuum-based models; (ii) why care must be taken when comparing IPR values from the different approaches, and (iii) further remarks on the normalization procedure outlined in the main text of the paper. We start our discussion with general comments on the calculation of IPR values.

Turning to our atomistic TB model, in general, the IPR value of a given TB wave function ψ_j can be calculated as follows:[7]

$$\mathrm{R}_j = \frac{\sum_i \left(\sum_\alpha |a_{i\alpha}|^2\right)^2}{\left(\sum_i \sum_\alpha |a_{i\alpha}|^2\right)^2}. \tag{A1}$$

Here, the sum over i runs over the N lattice sites/grid points in the simulation cell and $a_{i\alpha}$ are the expansion coefficients for a given basis state/orbital α of the wave function ψ_j at the lattice site/grid point i; in the sp^3 TB model, α denotes s, p_x, p_y, and p_z orbitals. For the continuum-based EMA description, a similar approach can be used and the sum becomes an integral,

$$\mathrm{R}_j = \frac{\int |\psi_j(\mathbf{x})|^4 d^3x}{\left[\int |\psi_j(\mathbf{x})|^2 d^3x\right]^2}. \tag{A2}$$

Please note, in the single-band EMA one is only left with one basis state, namely, an $|S\rangle$-like basis state. In general and based on the above expressions, the larger the IPR for a given state, the stronger the wave function localization effect. Using the TB model as an example, in the extreme case of a wave function localized to a single site/grid point, the IPR value based on Eq. (1) is $R_j = 1$. On the other hand, if the wave function is completely delocalized, thus distributed over the N lattice sites/grid points of the simulation cell, the IPR of such a state is $R_j = 1/N$; in the continuum case $R_j = 1/V$, with V being the volume of the system.

In the main text, we have studied the localization effects of electron and hole wave functions both in TB and the modified continuum-based models by means of IPR values. Overall, and as mentioned above that care must be taken when comparing the atomistic and continuum-based data for several reasons. First, the number of grid points/lattice sites differs between the Sphinx mesh and the atomistic model. Furthermore, as already discussed above, in the continuum-based models, a complete delocalized state for a given supercell would result in an IPR value of $R_{\mathrm{EMA}} = 1/V$, where V is the volume of the simulation cell. In the TB model, a complete delocalized state would have an IPR value of $R_{\mathrm{TB}} = 1/N$. Therefore, when comparing the lattice and continuum cases, the quantity we are calculating is different; thus, a "normalization procedure" needs to be established to connect N and V. Furthermore, it is important to note that the anion–cation structure is not resolved in the continuum-based models since they provide only an envelope function. We have found in previous work[7,64] that electron wave functions are mainly localized on the cation planes with a smaller probability density on the anion planes. The opposite is observed for the hole wave functions. Again, even for a completely delocalized state, this would have to be considered when comparing IPR values between TB and continuum-based models in general.

© Author(s) 2021

To account for these intrinsic differences while still being able to compare *trends* in the IPR values between the different methods, we use the average electron ground state IPR value (averaged over the ten different microscopic configurations) for the well with 5% In for calibration. We assume that on average the TB model and modified EMA$_S$, including CBE and VBE shifts, give very similar wave functions/localization effects for the electron ground state. In doing so, we can extract a "scaling factor" for the modified continuum-based models to account for the fundamental differences in these methods. The extracted scaling factor is then used for all other states and all other In contents since the volume of the supercells are kept approximately constant. Overall, the assumption that wave function localization aspects of the average electron ground state for the 5% In are very similar should be reasonable. This assumption is motivated by (i) (local) built-in field and strain effects are directly transferred into the continuum-based model, (ii) that previous calculations have already shown that the electron wave functions are less strongly affected by alloy fluctuations and that they reflect to a good first approximation an envelope function character,[7] and (iii) that we have chosen a low In content system as a reference point for which carrier localization effects in the electron wave function should even be less important. We note also that we have inspected charge densities of electron ground state wave functions for different configurations in the 5% In case and found a good agreement between those predicted by the continuum-based and the TB model. Having calibrated the EMA models in this way, any difference in the IPR values should mainly stem from differences in carrier localization effects.

DATA AVAILABILITY

The data that support the findings of this study are available from the corresponding author upon reasonable request.

REFERENCES

[1]A. Zakutayev, J. Mater. Chem. A **4**, 6742 (2016).
[2]C. J. Humphreys, MRS Bull. **33**, 459 (2008).
[3]F. A. Ponce, Nature **386**, 351 (1997).
[4]T. Liu, S. Jiao, H. Liang, T. Yang, D. Wang, and L. Zhao, RSC Adv. **5**, 33892 (2015).
[5]H. Amano, R. Collazo, C. de Santi, S. Einfeldt, M. Funato, J. Glaab, S. Hagedorn, A. Hirano, H. Hirayama, R. Ishii *et al.*, J. Phys. D: Appl. Phys. **53**, 503001 (2020).
[6]P. Dawson, S. Schulz, R. A. Oliver, M. J. Kappers, and C. J. Humphreys, J. Appl. Phys. **119**, 181505 (2016).
[7]D. S. P. Tanner, M. A. Caro, E. P. O'Reilly, and S. Schulz, RSC Adv. **6**, 64513 (2016).
[8]S. F. Chichibu, A. Uedono, T. Onuma, B. A. Haskell, A. Chakraborty, T. Koyama, P. T. Fini, S. Keller, S. P. DenBaars, J. S. Speck *et al.*, Nat. Mater. **5**, 810 (2006).
[9]D. M. Graham, A. Soltani-Vala, P. Dawson, M. J. Godfrey, T. M. Smeeton, J. S. Barnard, M. J. Kappers, C. J. Humphreys, and E. J. Thrush, J. Appl. Phys. **97**, 103508 (2005).
[10]C. M. Jones, C.-H. Teng, Q. Yan, P.-C. Ku, and E. Kioupakis, Appl. Phys. Lett. **111**, 113501 (2017).
[11]D. Watson-Parris, M. J. Godfrey, P. Dawson, R. A. Oliver, M. J. Galtrey, M. J. Kappers, and C. J. Humphreys, Phys. Rev. B **83**, 115321 (2011).
[12]S. Schulz, M. A. Caro, C. Coughlan, and E. P. O'Reilly, Phys. Rev. B **91**, 035439 (2015).
[13]M. Auf der Maur, A. Pecchia, G. Penazzi, W. Rodrigues, and A. Di Carlo, Phys. Rev. Lett. **116**, 027401 (2016).
[14]S. Schulz, D. P. Tanner, E. P. O'Reilly, M. A. Caro, T. L. Martin, P. A. J. Bagot, M. P. Moody, F. Tang, J. T. Griffiths, F. Oehler *et al.*, Phys. Rev. B **92**, 235419 (2015).
[15]D. S. P. Tanner and S. Schulz, Nanoscale **12**, 20258 (2020).
[16]Q. Liu, J. Lu, Z. Gao, L. Lai, R. Qin, H. Li, J. Zhou, and G. Li, Phys. Status Solidi B **247**, 109 (2010).
[17]T.-J. Yang, R. Shivaraman, J. S. Speck, and Y.-R. Wu, J. Appl. Phys. **116**, 113104 (2014).
[18]C.-K. Li, M. Piccardo, L.-S. Lu, S. Mayboroda, L. Martinelli, J. Peretti, J. S. Speck, C. Weisbuch, M. Filoche, and Y.-R. Wu, Phys. Rev. B **95**, 144206 (2017).
[19]M. A. der Maur, J. Green Eng. **5**, 133 (2016).
[20]M. Auf der Maur, J. Comput. Electron. **14**, 3981 (2015).
[21]J. Geng, P. Sarangapani, E. Nelson, C. Wordclman, B. Browne, T. Kubis, and G. Klimeck, in *2016 International Conference on Numerical Simulation of Optoelectronic Devices (NUSOD)* (IEEE, 2016), pp. 107–108.
[22]J. Geng, P. Sarangapani, K.-C. Wang, E. Nelson, B. Browne, C. Wordelman, J. Charles, Y. Chu, T. Kubis, and G. Klimeck, Phys. Status Solidi A **215**, 1700662 (2018).
[23]A. Di Vito, A. Pecchia, A. Di Carlo, and M. Auf der Maur, J. Appl. Phys. **128**, 041102 (2020).
[24]J. M. McMahon, D. S. P. Tanner, E. Kioupakis, and S. Schulz, Appl. Phys. Lett. **116**, 181104 (2020).
[25]O. Marquardt, D. Mourad, S. Schulz, T. Hickel, G. Czycholl, and J. Neugebauer, Phys. Rev. B **78**, 235302 (2008).
[26]P. Farrell, N. Rotundo, D. H. Doan, M. Kantner, J. Fuhrmann, and T. Koprucki, *Handbook of Optoelectronic Device Modeling and Simulation* (CRC Press, 2017), Vol. 2, p. 733.
[27]S. Schulz, O. Marquardt, C. Coughlan, M. A. Caro, O. Brandt, and E. P. O'Reilly, Proc. SPIE **9357**, 93570C (2015).
[28]P. R. C. Kent and A. Zunger, Appl. Phys. Lett. **79**, 1977 (2001).
[29]D. Thouless, Phys. Rep. **13**, 93–142 (1974).
[30]O. Marquardt, S. Schulz, C. Freysoldt, S. Boeck, T. Hickel, E. P. O'Reilly, and J. Neugebauer, Opt. Quant. Electron. **44**, 183 (2012).
[31]O. Marquardt, M. A. Caro, T. Koprucki, P. Mathé, and M. Willatzen, Phys. Rev. B **101**, 235147 (2020).
[32]O. Marquardt, S. Boeck, C. Freysoldt, T. Hickel, S. Schulz, J. Neugebauer, and E. P. O'Reilly, Comput. Mater. Sci. **95**, 280 (2014).
[33]O. Marquardt, E. P. O'Reilly, and S. Schulz, J. Phys.: Condens. Matter. **26**, 035303 (2013).
[34]M. Filoche, M. Piccardo, Y.-R. Wu, C.-K. Li, C. Weisbuch, and S. Mayboroda, Phys. Rev. B **95**, 144204 (2017).
[35]D. S. Tanner, P. Dawson, M. J. Kappers, R. A. Oliver, and S. Schulz, Phys. Rev. Appl. **13**, 044068 (2020).
[36]S. Schulz and G. Czycholl, Phys. Rev. B **72**, 165317 (2005).
[37]S. Schulz and G. Czycholl, Phys. Status Solidi C **3**, 1675 (2006).
[38]M. A. Caro, S. Schulz, and E. P. O'Reilly, Phys. Rev. B **88**, 214103 (2013).
[39]C. Coughlan, S. Schulz, M. A. Caro, and E. P. O'Reilly, Phys. Status Solidi B **252**, 879 (2015).
[40]S. Schulz, M. A. Caro, L.-T. Tan, P. J. Parbrook, R. W. Martin, and E. P. O'Reilly, Appl. Phys. Express **6**, 121001 (2013).
[41]E. P. O'Reilly, A. Lindsay, S. Tomic, and M. Kamal-Saadi, Semicond. Sci. Technol. **17**, 870 (2002).
[42]T. B. Boykin, N. Kharche, G. Klimeck, and M. Korkusinski, J. Phys.: Condens. Matter **19**, 036203 (2007).
[43]R. M. Martin, Phys. Rev. B **1**, 4005 (1970).
[44]S. Plimpton, J. Comput. Phys. **117**, 1 (1995).
[45]S. K. Patra and S. Schulz, Nano Lett. **20**, 234 (2020).
[46]M. Zielinski, Phys. Rev. B **86**, 115424 (2012).
[47]H. Si, ACM Trans. Math. Software **41**, 2629697 (2015).

© Author(s) 2021

[48]D. Chaudhuri, J. C. Kelleher, M. R. O'Brien, E. P. O'Reilly, and S. Schulz, Phys. Rev. B **101**, 035430 (2020).
[49]O. Marquardt, S. Boeck, C. Freysoldt, T. Hickel, and J. Neugebauer, Comput. Phys. Commun. **181**, 765 (2010).
[50]S. Boeck, C. Freysoldt, A. Dick, L. Ismer, and J. Neugebauer, Comput. Phys. Commun. **182**, 543 (2011).
[51]U. M. E. Christmas, A. D. Andreev, and D. A. Faux, J. Appl. Phys. **98**, 073522 (2005).
[52]P. Rinke, M. Winkelnkemper, A. Qteish, D. Bimberg, J. Neugebauer, and M. Scheffler, Phys. Rev. B **77**, 075202 (2008).
[53]O. Marquardt, S. Schulz, E. P. O'Reilly, C. Freysoldt, S. Boeck, T. Hickel, and J. Neugebauer, 2011 Numerical Simulation of Optoelectronic Devices, Rome (2011), pp. 111–112.
[54]S. Schulz, D. Chaudhuri, M. O'Donovan, S. K. Patra, T. Streckenbach, P. Farrell, O. Marquardt, and T. Koprucki, Proc. SPIE **11274**, 1127416 (2019).
[55]S. Adachi, *III-V Ternary and Quaternary Compounds* (Springer International Publishing, Cham, 2017), p. 1, ISBN: 978-3-319-48933-9.
[56]M. Winkelnkemper, A. Schliwa, and D. Bimberg, Phys. Rev. B **74**, 155322 (2006).
[57]K. Gawarecki and M. Zieliński, Phys. Rev. B **100**, 155409 (2019).
[58]S. Schulz, T. J. Badcock, M. A. Moram, P. Dawson, M. J. Kappers, C. J. Humphreys, and E. P. O'Reilly, Phys. Rev. B **82**, 125318 (2010).
[59]A. Morel, P. Lefebvre, S. Kalliakos, T. Taliercio, T. Bretagnon, and B. Gil, Phys. Rev. B **68**, 045331 (2003).
[60]P. G. Moses, M. Miao, Q. Yan, and C. G. Van de Walle, J. Chem. Phys. **134**, 084703 (2011).
[61]H. Ludwig, E. Runge, and R. Zimmermann, Phys. Rev. B **67**, 205302 (2003).
[62]F. Wegner, Z. Phys. B **36**, 209 (1980).
[63]L.-W. Wang, Phys. Rev. B **63**, 245107 (2001).
[64]S. Schulz, S. Schumacher, and G. Czycholl, Phys. Rev. B **73**, 245327 (2006).

© Author(s) 2021